APS physics

CHORUS

This is the accepted manuscript made available via CHORUS. The article has been published as:

Viscous reflection of internal waves from a slope

T. Kataoka and T. R. Akylas

Phys. Rev. Fluids **5**, 014803 — Published 13 January 2020

DOI: 10.1103/PhysRevFluids.5.014803

Viscous reflection of internal waves from a slope

T. Kataoka[1] and T. R. Akylas[2,*]

[1] *Faculty of Engineering, Kobe University, Rokkodai, Nada, Kobe 657-8501, Japan*

[2] *Department of Mechanical Engineering, Massachusetts Institute of Technology, Cambridge, Massachusetts 02139, USA*

Motivated by the laboratory experiments of Rodenborn et al. [Physics of Fluids **23**, 026601 (2011)], a weakly nonlinear model is developed that accounts for viscous dissipation in the reflection of a finite-width internal wave beam from a uniform slope. Asymptotically, at high Reynolds number, viscous effects come into play predominantly in the immediate vicinity of the critical slope angle equal to the propagation angle to the horizontal of the incident wave beam. However, in the experiments of Rodenborn et al. where the Reynolds number is moderately large, it turns out that viscosity is important throughout the slope range considered, which explains the overall poor agreement of their observations with earlier inviscid models. The predictions of the proposed model, by contrast, are in good qualitative, and in some respects quantitative, agreement with these experiments and also they compare favorably against numerical Navier–Stokes simulations.

I. INTRODUCTION

Internal gravity wave propagation in continuously stratified fluids is anisotropic due to gravity which provides a preferred direction. This inherent anisotropy manifests, among

* Corresponding author: trakylas@mit.edu

other interesting phenomena, in the way internal waves reflect at sloping boundaries: incident and reflected wave rays make the same angle to the direction of gravity [1], rather than the direction perpendicular to the boundary as would be the case for isotropic wave motion. As a result of this unusual rule, wavelengths are reduced when internal waves reflect from a slope in the upslope direction [1]. Thus, upon upslope reflection, energy is transferred to smaller scales – a focusing effect that promotes instabilities and mixing close to boundaries [2, 3] – which supports the belief that internal wave reflections by topography play a part in the redistribution and eventual dissipation of tidal energy in the ocean [4, 5].

This focusing due to reflection is most dramatic when the angle of incidence to the horizontal matches the boundary slope: at this critical condition, the reflected wavelength tends to zero while the velocity amplitude becomes infinite. This singular behavior that follows from linear inviscid considerations [1], was reexamined by Dauxois and Young [6] using a weakly nonlinear, slightly viscous approach for a reflecting nearly monochromatic sinusoidal plane wave. They came to the conclusion that near-critical reflection may lead to overturning of the isopycnals close to the slope, suggesting the occurrence of convective instability, which has been confirmed experimentally [7] and numerically [8]. An asymptotic theory for near-critical reflection of a plane wave beam with locally confined spatial profile [9] was developed by Tabaei [10], following a similar approach to Ref. [6] but under the assumption of inviscid flow.

Another notable feature of internal wave reflections is the generation of higher harmonics due to nonlinear interactions of the incident and reflected waves. This type of interaction was first studied theoretically assuming weakly nonlinear sinusoidal plane waves in an in-

viscid fluid, by Thorpe [11], who pointed attention to certain special configurations where resonances of the induced second- and third-harmonic waves are possible. These resonances were revisited in very recent theoretical and numerical work [12], which indicates that, unlike monochromatic sinusoidal waves, in the case of finite-width wave beams the resonant response is bounded. Furthermore, when the boundary slope is increased towards critical, viscous dissipation dominates over the energy transfer to the second harmonic due to nonlinear interactions.

Aside from possible resonances, however, reflections of internal wave beams with locally confined profile are generally accompanied by radiating higher harmonics. Such secondary reflected beams were brought out by numerical simulations of the ocean internal tide [13], which prompted Tabaei et al. [14] to propose a weakly nonlinear inviscid model for the reflection of a locally confined beam with constant frequency ω from a uniform slope. According to this model, the leading-order (quadratic) nonlinear interactions in the overlap region of the incident and the primary reflected beam drive a mean-flow and a second-harmonic disturbance; the former stays in the vicinity of the slope while the latter, assuming 2ω is less than the background buoyancy frequency, radiates away along a direction specified by the dispersion relation. These predictions are consistent with laboratory experiments [15, 16] as well as numerical simulations [17, 18].

The main motivation for the present paper comes from the experimental and numerical study by Rodenborn et al. [19] (hereafter referred to as RKZS), which aimed at quantitative comparison with the analyses of Thorpe [11] and Tabaei et al. [14]. Their laboratory experimental setup used a moving-plate wave generator [20, 21] at one end of a tank to excite a

finite-width wave beam with prescribed profile and frequency which travelled along the tank at the angle $\theta = 22.7^\circ$ to the horizontal in keeping with the dispersion relation. The beam was then reflected from an inclined plate at the other end of the tank, and by varying the plate inclination α to the horizontal, RKZS made a systematic study of the strength of the radiated second harmonic as a function of the boundary slope in the range $0 < \alpha < 30^\circ$. The experimental observations, however, did not corroborate the theoretical predictions for the slope that gives the strongest second-harmonic response. According to Tabaei et al. [14] this maximum would be expected at the critical condition $\alpha = \theta = 22.7^\circ$, where the (inviscid) theoretical response features an infinite resonance peak. Instead, the experimental second-harmonic response is a bell-shaped curve with peak at $\alpha = 13.2^\circ$, which is also quite different from 8.2°, the slope angle at which second-harmonic resonance is predicted by Thorpe [11] for a sinusoidal wave incident at $\theta = 22.7^\circ$. Furthermore, RKZS conducted numerical Navier–Stokes simulations for various incident-beam peak amplitudes and fluid viscosities. These numerical results support the experimental observations and, moreover, appear to suggest that the poor agreement with the model by Tabaei et al. [14] is due to the weakly nonlinear assumption which limits the validity of the model to very small-amplitude incident beams, weaker than those measurable experimentally.

Here, we reexamine the experimental observations of RKZS in the light of a weakly nonlinear model that includes the dominant effects of viscous dissipation in the reflection of an internal wave from a slope. In view of the experimental setup of RKZS, our analysis focuses on finite-width wave beams and is distinct from an earlier viscous treatment of reflecting modulated wavetrains [22]. It is argued that viscous effects cannot be ignored close to the

critical condition $\alpha = \theta$, and the range of near-critical slope angles where dissipation plays an essential part is controlled by the flow Reynolds number. Under the experimental flow conditions of RKZS, in particular, we find that viscosity is important throughout the slope range $0 < \alpha < 30^\circ$, while for Reynolds number 10 times the experimental value this range shrinks to $10^\circ \lesssim \alpha < 30^\circ$. Thus, the main reason for the poor agreement between the experimental observations and the model of Tabaei et al. [14] is viscous dissipation, in contrast to the incident-beam amplitude which is a secondary factor. In addition, our theoretical results for the primary- and second-harmonic responses compare favorably against numerical Navier–Stokes simulations. Specifically, in regard to the strength of the radiated second-harmonic beam, the present model predicts a maximum close to the experimental value $\alpha = 13.2^\circ$. Furthermore, the theoretical estimates for the 'intensity' defined in RKZS to measure the second-harmonic response show similar qualitative behavior to the observations as the slope is varied. Quantitatively, however, they are an order of magnitude smaller (by a constant scaling factor) than the experimental ones (reported in Fig. 7 of RKZS); the reason for this discrepancy is not known.

II. VISCOUS SCALINGS

Apart from assuming a viscous fluid (kinematic viscosity ν_*), the present formulation parallels that of the inviscid model in Tabaei et al. [14]. Specifically, we consider the reflection of internal waves from a rigid slope (constant angle α to the horizontal) in a non-rotating, incompressible, uniformly stratified Boussinesq fluid (constant buoyancy frequency N_*). Furthermore, there are no variations along the slope isobaths (transverse direction) so the flow is

two-dimensional. Under these flow conditions, employing a slope-oriented coordinate system with x in the upslope direction and y perpendicular to the slope (see Fig. 1), the streamfunction $\psi(x, y, t)$ and the reduced density $\rho(x, y, t)$ are governed by the dimensionless equations

$$\rho_t + \psi_x \cos\alpha - \psi_y \sin\alpha + J(\rho, \psi) = 0, \tag{1a}$$

$$\nabla^2\psi_t - \rho_x \cos\alpha + \rho_y \sin\alpha + J(\nabla^2\psi, \psi) = \frac{1}{\mathrm{Re}}\nabla^4\psi, \tag{1b}$$

where $J(a, b) = a_x b_y - a_y b_x$ is the Jacobian. To make variables dimensionless, we have used the time scale $1/N^*$ and a characteristic wave length L_* (to be specified later). Based on these scales, the Reynolds number is defined as

$$\mathrm{Re} = \frac{N_* L_*^2}{\nu_*}. \tag{2}$$

Furthermore, for a viscous fluid, the tangential $u = \psi_y$ and the normal $v = -\psi_x$ to the slope velocity components vanish on the slope

$$\psi_x = \psi_y = 0 \qquad (y = 0). \tag{3}$$

Before discussing the nonlinear reflection of internal wave beams, it is useful to estimate the effects of viscosity on the linear reflection of a sinusoidal plane wave. To this end, we

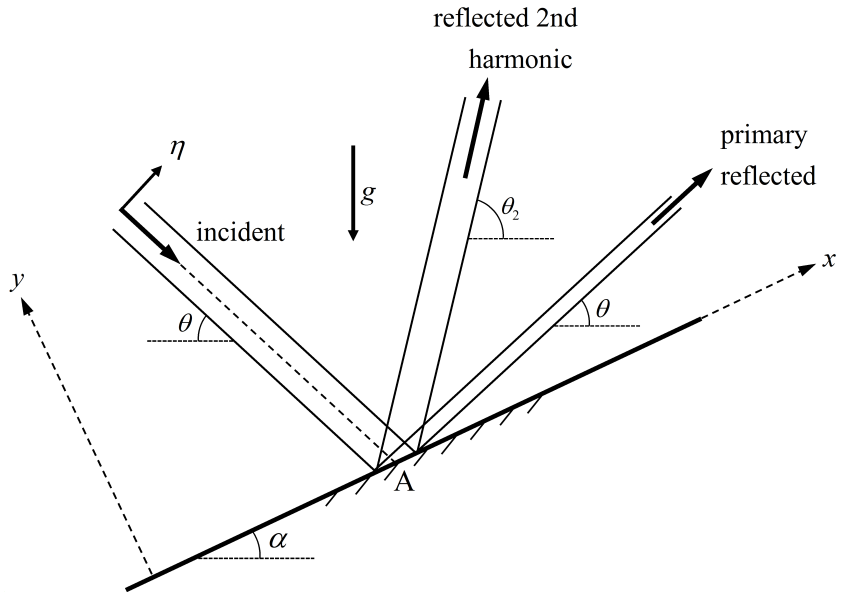

FIG. 1. Geometry of internal wave beam reflection from a slope of angle α, for the case when the incident beam hits the slope at an angle $\theta < \alpha$, to the horizontal. The primary reflected beam is also inclined to the horizontal by θ, while the radiated second-harmonic beam stretches along θ_2 to the horizontal, where $\sin\theta_2 = 2\sin\theta < 1$.

consider disturbances in the form

$$(\psi, \rho) \propto \mathrm{e}^{\mathrm{i}l(x+my)}\mathrm{e}^{-\mathrm{i}\omega t}, \tag{4}$$

where the frequency ω and the upslope wavenumber l are taken to be real while m, which controls the behavior normal to the slope, is possibly complex. (For algebraic convenience, rather than the wavenumber normal to the slope, here we work with m, the ratio of the normal to the tangential wavenumber.) Upon substitution of expressions (4) into Eqs.(1), ignoring the nonlinear terms, it is found that

$$m^2(\omega^2 - \sin^2\alpha) + m\sin 2\alpha - \cos^2\alpha + \omega^2 + \frac{\mathrm{i}}{\mathrm{Re}}\omega l^2(1+m^2)^2 = 0. \tag{5}$$

In the inviscid limit ($\mathrm{Re} \to \infty$), Eq.(5) reduces to the familiar internal wave dispersion relation which is quadratic in m. For given $0 < \omega = \sin\theta < 1$ and $l > 0$ the two (real) roots

$$m_{\mathrm{inc}} = \cot(\alpha + \theta), \quad m_{\mathrm{refl}} = -\cot(\theta - \alpha) \tag{6}$$

then correspond to an incident and a reflected wave at the angle θ to the horizontal (see Fig. 1). These two waves can be readily combined to satisfy the inviscid condition $v = -\psi_x = 0$ on the slope $y = 0$

$$\psi = \mathrm{e}^{\mathrm{i}lx}\left\{\mathrm{e}^{\mathrm{i}lm_{\mathrm{inc}}y} - \mathrm{e}^{\mathrm{i}lm_{\mathrm{refl}}y}\right\}\mathrm{e}^{-\mathrm{i}\omega t} + \mathrm{c.c.}. \tag{7}$$

For finite Re, by contrast, Eq.(5) is quartic in m and has four roots $m = m_1, \cdots, m_4$. Assuming $\mathrm{Re} \gg 1$, m_1 and m_2 are slightly perturbed from the inviscid roots in Eq.(6),

$$m_1 = m_{\mathrm{inc}} - \mathrm{i}\frac{s_1}{\mathrm{Re}} + \cdots, \quad m_2 = m_{\mathrm{refl}} + \mathrm{i}\frac{s_2}{\mathrm{Re}} + \cdots, \tag{8a}$$

where

$$s_1 = \frac{l^2}{2\cos\theta\sin^4(\alpha+\theta)}, \quad s_2 = \frac{l^2}{2\cos\theta\sin^4(\theta-\alpha)}. \tag{8b}$$

Since $\mathrm{Im}\{lm_1\} < 0$ and $\mathrm{Im}\{lm_2\} > 0$, viscous dissipation attenuates the incident/reflected wave as it approaches/leaves the slope, in keeping with causality. The other two roots of

Eq.(5) are of purely viscous origin

$$m_{3,4} \sim s_{\pm} \mathrm{Re}^{1/2}, \tag{9a}$$

where

$$s_{\pm} = \pm \frac{(1+\mathrm{i})}{\sqrt{2}} \frac{(\sin^2\theta - \sin^2\alpha)^{1/2}}{l\sqrt{\sin\theta}}. \tag{9b}$$

Out of these, only the root associated with exponential decay for $y \gg 1$ is relevant here and results in a disturbance that is confined in $y = O(\mathrm{Re}^{-1/2})$. This boundary-layer solution can be combined with the incident and reflected waves corresponding to m_1 and m_2 in Eqs.(8), to satisfy the viscous boundary conditions (3). Specifically, for $\theta > \alpha$, the viscous counterpart of the inviscid reflection in Eq.(3) takes the form

$$\psi = \mathrm{e}^{\mathrm{i}lx} \left\{ \mathrm{e}^{\mathrm{i}lm_1 y} + R\,\mathrm{e}^{\mathrm{i}lm_2 y} - (1+R)\mathrm{e}^{\mathrm{i}ls_+ \mathrm{Re}^{1/2} y} \right\} \mathrm{e}^{-\mathrm{i}\omega t} + \mathrm{c.c.}, \tag{10a}$$

where

$$R = -1 + \frac{m_{\mathrm{inc}} - m_{\mathrm{refl}}}{s_+ \mathrm{Re}^{1/2}} + \cdots . \tag{10b}$$

Thus, in addition to introducing an $O(\mathrm{Re}^{-1/2})$ boundary layer next to the slope, viscosity makes an $O(\mathrm{Re}^{-1/2})$ correction to the reflection coefficient R from its inviscid value of -1 in Eq.(7).

The effect of viscosity becomes far more pronounced, however, if the angle of incidence θ is close to the slope angle α. This is to be expected because at the critical angle $\theta = \alpha$ the inviscid reflection is singular: $m_{\mathrm{refl}} \to \infty$ as $\theta \to \alpha$ according to Eq.(6). As a result, the reflected wave, which in this limit propagates along the slope, features vanishingly small

wavelength and the upslope flow velocity $\psi_y \to \infty$. Viscosity heals this singular behavior by ensuring that the reflected wavenumber m_2 remains finite, but large, when $\theta \approx \alpha$ and $\mathrm{Re} \gg 1$. Specifically, returning to Eqs.(8), for $|\theta - \alpha| = \delta \ll 1$, the $O(1/\mathrm{Re})$ contribution to m_2 becomes $O(1/\delta^4 \mathrm{Re})$, so when $\delta = O(\mathrm{Re}^{-1/3})$ this viscous correction is comparable to the inviscid reflected wavenumber $m_{\mathrm{refl}} = O(1/\delta)$. Thus, in the near-critical range

$$\alpha = \theta + \sigma \mathrm{Re}^{-1/3}, \tag{11}$$

where $\sigma = O(1)$, viscous effects come to center stage and no longer can be treated as a small perturbation.

This elevated role of viscosity is also evident from the characteristic equation (5). In the near-critical reflection range defined by Eq.(11), for $\mathrm{Re} \gg 1$, $m_1 = m_{\mathrm{inc}} + O(1/\mathrm{Re})$ as given in Eq.(8a) is still a root of Eq.(5) and corresponds to the incident, nearly inviscid wave; the other three roots, however, are controlled by Re

$$m \sim \frac{p}{l} \mathrm{Re}^{1/3}, \tag{12a}$$

where p satisfies

$$\frac{\mathrm{i}}{2\cos\theta} p^3 - \sigma p + l = 0. \tag{12b}$$

Two of the roots of this cubic have $\mathrm{Im}\{p\} > 0$, consistent with decaying behavior away from the slope ($y \gg 1$); one of these corresponds to an $O(\mathrm{Re}^{-1/3})$ viscous boundary layer and the other to the reflected wave, which is confined in an $O(\mathrm{Re}^{-1/3})$ region next to the slope. These two disturbances can be combined with the incident wave to satisfy the boundary conditions

(3) on the slope.

From the discussion above, for $\mathrm{Re} \gg 1$ inviscid analysis is expected to provide a good approximation to internal wave reflection only if the incidence angle θ is not too close to the slope angle α; that is, in view of Eq.(11), only if the condition $|\sigma| \gg 1$, or

$$|\alpha - \theta| \gg \mathrm{Re}^{-1/3}, \tag{13}$$

is also met. Thus, depending on how large Re is, there is a range of incidence angles near the critical $\theta = \alpha$ for which viscous effects cannot be ignored. For instance, in the experimental setup of RKZS, $N_* = 1.63\,\mathrm{rad/s}$, $\nu_* = 0.01\,\mathrm{cm}^2/\mathrm{s}$ and taking the length scale $L_* = 5\,\mathrm{cm}/2\pi$ (carrier wavelength/2π of the incident wave beam), we find $\mathrm{Re} = 103$ so $\mathrm{Re}^{-1/3} = 0.21$. Furthermore, in these experiments, the slope angle was varied in the range $0 \leq \alpha \leq \theta$ for three incidence angles $\theta = 15^\circ, 22.7^\circ, 28^\circ$, so $|\alpha - \theta| \leq 0.49$ radians. Under these flow conditions, the inviscid criterion in Eq.(13) is met rather marginally even at the extreme $\alpha = 0$, and viscous effects are likely to be important throughout the slope range $0 \leq \alpha \leq \theta$. This claim is supported by the theoretical model and numerical simulations discussed below (see Sec.V).

III. NEAR-CRITICAL BEAM REFLECTION

Motivated by the above qualitative discussion, we now develop a weakly nonlinear theory for near-critical reflection of internal wave beams, accounting for viscous effects when $\mathrm{Re} \gg 1$ under the scaling in Eq.(11). Our approach blends the inviscid analysis of this problem presented in Tabaei [10] with the slightly viscous treatment of near-critical reflection of a

sinusoidal plane wave in Dauxois and Young [6]. In view of these earlier closely related studies, only the main steps of the present analysis will be highlighted.

Assuming steady state, the incident wave beam is a superposition of sinusoidal waves of the form in Eq.(4) having the same frequency $\omega = \sin\theta$, which fixes the angle of incidence θ,

$$\psi^{\rm inc} = \varepsilon \left\{ Q^{\rm inc}(x,y) \mathrm{e}^{-\mathrm{i}\omega t} + \text{c.c.} \right\}, \tag{14}$$

where

$$Q^{\rm inc}(x,y) = \int_0^\infty \mathrm{d}l A(l) \exp\left\{ \mathrm{i}l(x + m_1 y) \right\} \tag{15}$$

and $m_1 = \cot(\theta + \alpha) + O(1/\mathrm{Re})$ in accordance with Eq.(8a). Here, $A(l)$ is a prescribed function that controls the beam profile and $\varepsilon = U_*/N_*L_* \ll 1$ is an amplitude parameter that measures nonlinearity, where U_* is a characteristic velocity in the incident beam.

Turning next to the reflected wave beam, our discussion in Sec.II suggests that viscosity has an $O(1)$ effect on near-critical reflection, namely when $|\alpha - \theta| \lesssim O(\mathrm{Re}^{-1/3})$. Furthermore, under these flow conditions, the reflected disturbance forms an $O(\mathrm{Re}^{-1/3})$ thick boundary layer next to the slope. However, when θ is close to α ($|\alpha - \theta| = \delta \ll 1$) nonlinearity is also expected to come into play because, according to Eq.(6), the inviscid wavenumber normal to the slope $m_{\rm refl} = O(1/\delta) \gg 1$. As a result, the reflected beam behaves as a boundary layer, whose thickness is $O(\delta)$. Furthermore, the upslope beam velocity ψ_y as well as the density ρ of the reflected beam become $O(\varepsilon/\delta)$ and are large relative to the $O(\varepsilon)$ incident wave beam. This resonant behavior, in turn, amplifies the interaction of the reflected beam with the $O(\varepsilon^2/\delta^2)$

second-harmonic ($\propto \mathrm{e}^{-2\mathrm{i}\omega t}$) and mean-flow disturbances induced by quadratic interactions of the incident and reflected beams near the slope.

As shown in Refs. [6, 10], this nonlinear interaction mechanism can have an $O(1)$ effect on the upslope evolution of the reflected beam profile when $\delta = |\alpha - \theta| \lesssim O(\varepsilon^{2/3})$. Thus, at near-critical reflection, nonlinearity and viscosity are equally important if $\mathrm{Re}^{-1/3} \sim \varepsilon^{2/3}$. This balance is achieved by taking

$$\frac{1}{\mathrm{Re}} = \nu\varepsilon^2, \tag{16}$$

where $\nu = O(1)$. Then, the near-critical reflection range defined by Eq.(11) may alternatively be expressed in terms of ε

$$\alpha = \theta + \tilde{\sigma}\varepsilon^{2/3}, \tag{17}$$

where $\tilde{\sigma} = \sigma\nu^{1/3} = O(1)$.

Under the above scalings, we now focus on the boundary layer that forms next to the slope and contains the reflected wave beam. Employing the boundary-layer coordinate $Y = \varepsilon^{-2/3}y$, $\psi(x, Y, t)$ and $r(x, Y, t) = \varepsilon^{2/3}\rho$ are expanded as follows

$$\psi = \varepsilon\psi_1 + \varepsilon^{4/3}\psi_2 + \varepsilon^{5/3}\psi_3 + \cdots, \tag{18a}$$

$$r = \varepsilon r_1 + \varepsilon^{4/3} r_2 + \varepsilon^{5/3} r_3 + \cdots. \tag{18b}$$

Here, ρ has been re-scaled to account for the resonant behavior of $\rho = O(\varepsilon/\delta) = O(\varepsilon^{1/3})$ in the near-critical range $\delta = O(\varepsilon^{2/3})$ defined in Eq.(17). Substituting these expansions in

Eqs.(1), to leading order, we obtain

$$\psi_1 = q(x,Y)\mathrm{e}^{-\mathrm{i}\omega t} + \text{c.c.}, \tag{19a}$$

$$r_1 = \mathrm{i}q_Y\mathrm{e}^{-\mathrm{i}\omega t} + \text{c.c.}. \tag{19b}$$

Here, $q(x,Y)$ is the yet undetermined boundary layer profile which must also satisfy the boundary conditions (3) on the slope

$$q_x = q_Y = 0 \quad (Y = 0). \tag{20}$$

In addition, matching of the boundary-layer solution in Eq.(19a) with the incident wave in Eq.(14) at the outer edge of the boundary layer requires that

$$\lim_{Y\to\infty} q = Q^{\text{inc}}(x, y = 0). \tag{21}$$

Proceeding to the next order, from the $O(\varepsilon^{2/3})$ terms in Eq.(1a) and the $O(1)$ terms in Eq.(1b), along with using Eqs.(19), we find that

$$\psi_2 = \left\{\frac{\mathrm{i}}{\omega}\int_0^Y \mathrm{d}Y' J(q, q_{Y'})\mathrm{e}^{-2\mathrm{i}\omega t} + \text{c.c.}\right\} + \frac{\mathrm{i}}{\omega}J(q, q^*), \tag{22a}$$

$$r_2 = \frac{1}{\omega}\left\{J(q_Y, q)\mathrm{e}^{-2\mathrm{i}\omega t} + J(q, q_Y^*)\right\} + \text{c.c.}. \tag{22b}$$

It should be noted that both the second-harmonic and the mean-flow components of ψ_2 above automatically satisfy the boundary conditions (3) on the slope ($Y = 0$) since q does so according to Eq.(20). In regard to the far-field behavior of ψ_2, using the matching condition

in Eq.(21), it is clear that the induced mean flow vanishes as $Y \to \infty$, so it does not extend beyond the boundary layer. The induced second harmonic, however, approaches a finite limit for $Y \gg 1$

$$\psi_2 \sim \frac{\mathrm{i}}{\omega} \int_0^\infty \mathrm{d}Y' J(q, q_{Y'}) \mathrm{e}^{-2\mathrm{i}\omega t} + \text{c.c.}. \tag{23}$$

Thus, to achieve matching, it is necessary to allow for a second-harmonic reflected disturbance far from the slope ($y = O(1)$). This 'outer' response is driven by quadratic interactions in the boundary layer and in the case $2\omega < 1$ takes the form of a radiating beam. We shall return to this point in Sec.IV.

To determine the boundary-layer profile $q(x, Y)$, we return to Eqs.(1) and collect primary-harmonic ($\propto \mathrm{e}^{-\mathrm{i}\omega t}$) terms to the next order, namely $O(\varepsilon)$ in Eq.(1a) and $O(\varepsilon^{1/3})$ in Eq.(1b). These terms also include contributions from the interaction of the leading-order disturbance in Eqs.(19) with the induced second-harmonic and mean-flow corrections in Eqs.(22). However, similar to the analyses in Refs. [6, 10], after significant algebra it turns out that these nonlinear (cubic) terms cancel out, leaving the following linear evolution equation for q

$$\frac{\mathrm{i}\nu}{2\cos\theta} q_{YYYY} + \tilde{\sigma} q_{YY} - q_{xY} = 0. \tag{24}$$

This equation is solved by taking Fourier transform in x

$$\frac{\mathrm{i}\nu}{2\cos\theta} \hat{q}_{YYYY} + \tilde{\sigma} \hat{q}_{YY} - \mathrm{i}l\hat{q}_Y = 0, \tag{25}$$

along with the boundary conditions in Eq.(20)

$$\hat{q} = \hat{q}_Y = 0 \quad (Y = 0), \tag{26}$$

and the matching condition in Eq.(21)

$$\lim_{Y\to\infty} \hat{q} = \hat{Q}^{\mathrm{inc}}(l, y = 0), \tag{27}$$

where

$$q(x, y) = \int_{-\infty}^{\infty} \mathrm{d}l \mathrm{e}^{\mathrm{i}lx} \hat{q}(l, Y). \tag{28}$$

Furthermore, Eq.(15) indicates that

$$\hat{Q}^{\mathrm{inc}}(l, 0) = A(l) \quad (l > 0), \quad \hat{Q}^{\mathrm{inc}}(l, 0) = 0 \quad (l < 0). \tag{29}$$

In view of Eq.(29), the solution to the boundary-value problem for $\hat{q}(l, Y)$ governed by Eqs.(25)–(27) takes the form

$$\hat{q} = A(l) \left\{ 1 + \frac{\tilde{p}_1 \exp(\mathrm{i}\tilde{p}_2 Y) - \tilde{p}_2 \exp(\mathrm{i}\tilde{p}_1 Y)}{\tilde{p}_2 - \tilde{p}_1} \right\} \quad (l > 0), \tag{30a}$$

$$\hat{q} = 0 \quad (l < 0), \tag{30b}$$

where $\tilde{p}_{1,2}$ are the roots of the cubic equation

$$\frac{\mathrm{i}\nu}{2\cos\theta}\tilde{p}^3 - \tilde{\sigma}\tilde{p} + l = 0 \tag{31}$$

with $\mathrm{Im}\{\tilde{p}_{1,2}\} > 0$, in keeping with the matching condition (27). Recalling that $\tilde{\sigma} = \sigma\nu^{1/3}$, where $\nu = 1/(\mathrm{Re}\varepsilon^2)$ according to Eq.(16), these roots are related to those of the cubic in Eq.(12b) via $\tilde{p}_{1,2} = \nu^{-1/3}p_{1,2}$.

Finally, upon inverting the Fourier transform in Eq.(28) with $\hat{q}$ given by Eqs.(30) and making use of Eqs.(14) and (15), the overall solution for the incident and the (primary) reflected beam can be expressed as

$$\psi = \varepsilon Q_1(x,y)\mathrm{e}^{-\mathrm{i}\omega t} + \mathrm{c.c.}, \tag{32a}$$

where

$$Q_1(x,y) = Q^{\mathrm{inc}}(x,y) + \int_0^\infty \mathrm{d}l\mathrm{e}^{\mathrm{i}lx}A(l)\frac{p_1\exp(\mathrm{iRe}^{1/3}p_2y) - p_2\exp(\mathrm{iRe}^{1/3}p_1y)}{p_2 - p_1}. \tag{32b}$$

Since the leading-order nonlinear terms in Eq.(24) drop out, this linear viscous solution is expected to be also valid for small but finite ε.

IV. RADIATED SECOND HARMONIC

While the primary reflected beam is not affected by nonlinearity to leading order, quadratic nonlinear interactions between this and the incident beam give rise to a second-harmonic reflected disturbance that extends away from the slope. Furthermore, if $2\omega < 1$ this nonlinear feature manifests as a radiating beam at the angle θ_2, where $2\omega = \sin\theta_2$ (see Fig. 1). Based on

the asymptotic theory outlined in Sec.III, it is possible to compute the radiating beam profile via matching with the second-harmonic response at the outer edge of the boundary layer ($Y \gg 1$) in Eq.(23). In this asymptotic approach, as the angle θ_2 is far from critical, viscous effects on the second-harmonic beam propagation would be entirely absent because in the limit $\mathrm{Re} \gg 1$ they are of higher order in comparison with the near-critical primary reflected beam. However, in situations such as the experiments of RKZS where Re is moderately large, evidently, the induced second-harmonic beam is attenuated away from the slope due to viscous dissipation.

To allow for this possibility, rather than employing asymptotic matching, we shall compute the radiated second harmonic directly from Eqs.(1), using Eqs.(32) to estimate the quadratic interactions of the incident and the primary-harmonic reflected beam. Specifically, assuming $0 < \varepsilon \ll 1$, we first expand ψ in harmonics

$$\psi = \varepsilon \left\{ Q_1(x,y)\mathrm{e}^{-\mathrm{i}\omega t} + \mathrm{c.c.} \right\} + \varepsilon^2 \left\{ Q_2(x,y)\mathrm{e}^{-2\mathrm{i}\omega t} + \mathrm{c.c.} \right\} + \cdots \tag{33}$$

with an analogous expansion for ρ, where the $O(\varepsilon)$ term accounts for the incident and the primary-harmonic reflected beam in Eqs.(32). These expansions are then substituted into Eqs.(1) with the viscous term in Eq.(1b) intact. Upon collecting second-harmonic ($\propto \mathrm{e}^{-2\mathrm{i}\omega t}$) terms, after some algebra, we obtain the following equation for the second-harmonic profile Q_2

$$\left(4\omega^2 - \sin^2\alpha\right) Q_{2yy} + \sin 2\alpha\, Q_{2xy} + \left(4\omega^2 - \cos^2\alpha\right) Q_{2xx} - \frac{2\mathrm{i}}{\mathrm{Re}}\omega\nabla^4 Q_2 = f, \tag{34}$$

where

$$f = \mathrm{i}\omega \left\{ -2J(\nabla^2 Q_1, Q_1) + \frac{\partial}{\partial \chi} J(Q_{1\chi}, Q_1) \right\}, \tag{35}$$

with $\partial/\partial\chi \equiv \mathrm{i}\,(\cos\alpha\,\partial/\partial x - \sin\alpha\,\partial/\partial y)/\sin\theta$. As expected, the forcing term $f(x,y)$ in Eq.(35) derives from quadratic interactions of the incident and the primary reflected beam near the slope. In addition, Q_2 must obey the boundary conditions (3) on the slope

$$Q_{2x} = Q_{2y} = 0 \quad (y = 0) \tag{36}$$

and should also decay far from the slope

$$Q_2 \to 0 \quad (y \to \infty). \tag{37}$$

The above boundary-value problem for Q_2 is tackled by a similar procedure to that followed earlier for solving Eqs.(25)–(27) that govern the primary reflected beam. Briefly, taking Fourier transform in x as before, Eq.(34) becomes

$$\left(4\omega^2 - \sin^2\alpha\right)\hat{Q}_{2yy} + \mathrm{i}l\sin 2\alpha\,\hat{Q}_{2y} - l^2\left(4\omega^2 - \cos^2\alpha\right)\hat{Q}_2 - \frac{2\mathrm{i}\omega}{\mathrm{Re}}\left(\frac{\mathrm{d}^2}{\mathrm{d}y^2} - l^2\right)^2 \hat{Q}_2 = \hat{f}. \tag{38}$$

Since Q_1 in Eq.(32b) involves $l > 0$ only ($\hat{Q}_1 = 0$ for $l < 0$), $\hat{f} = 0$ for $l < 0$; hence, $\hat{Q}_2 = 0$ for $l < 0$ as well. Focusing then on $l > 0$, the characteristic equation for determining homogeneous solutions ($\propto \mathrm{e}^{\mathrm{i}l\tilde{m}y}$) of the ordinary differential equation (38) is readily deduced from Eq.(5) by letting $\omega \to 2\omega = \sin\theta_2$, $m \to \tilde{m}$. Out of the four characteristic roots,

only two are consistent with the causality condition (37), one corresponding to a radiating wave attenuated by viscosity at the angle θ_2 and the other to a boundary-layer disturbance confined near the slope. These two homogeneous solutions are combined with a particular solution of Eq.(38) that decays as $y \to \infty$ (obtained via variation of parameters) to satisfy the boundary conditions (36) on the slope. Finally, once $\hat{Q}_2(l, y)$ is computed as outlined above, the second-harmonic profile $Q_2(x, y)$ is found by inverting the Fourier transform similar to Eq.(28).

V. RESULTS AND DISCUSSION

We now apply our theoretical model to an incident wave beam whose profile $Q^{\rm inc} + \text{c.c.}$ in Eq.(14) consists of a sinusoid (with wavelength normalized to 2π, which fixes the characteristic length L_*) multiplied by the Gaussian $\exp\left(-(\eta/4.4)^2\right)$, where η denotes the (dimensionless) across-beam coordinate (Fig. 1). For $L_* = 5\text{cm}/2\pi$, this incident beam profile mimics the one generated in RKZS. Furthermore, the amplitude parameter $\varepsilon = U_*/N_*L_*$ is defined with the maximum beam velocity as U_*. In the experiment of RKZS, where $N_* = 1.63\,\text{rad/s}$ and $U_* = 0.25\,\text{cm/s}$, $\varepsilon = 0.2$.

For comparison against the theoretical predictions, we also conducted numerical simulations of the reflection of incident wave beams with the profile specified above. The simulations are based on the Navier–Stokes equations subject to no-slip conditions on the slope as in Eq.(3), and with a suitable forcing term added on the right-hand side of the momentum equation to drive the incident wave. The numerical solution procedure is similar to the MAC method introduced in Harlow and Welch [23]. It focuses on the Poisson equation for

the pressure that follows from taking the divergence of the momentum equation and applying continuity. The flow field is obtained by solving this Poisson equation iteratively until convergence. Spatial discretization is carried out using third-order upwind and second-order centered finite differences for the convective and the viscous terms, respectively. The computational domain is taken to be wide enough ($-380 < x < 380$, $0 < y < 130$) such that during the computation artificial reflections at the boundaries do not interfere with the beam reflection from the slope. Furthermore, to improve resolution, grid points (typically 600×600 in $x \times y$) are spaced unevenly, with higher concentration in the overlap region of the incident and the reflected waves as well as in the boundary layer along the slope. Time stepping is made by a predictor–corrector scheme with $\Delta t = 0.015$. The computation is continued until steady state is reached to a reasonable approximation, which typically takes $20 - 30$ wave beam periods.

A. Primary reflected wave

Figure 2 shows plots, for different Re and ε, of the amplitude of the primary-harmonic reflected beam $A_{\rm prim}$ (normalized with the incident beam amplitude ε) at fixed angle of incidence $\theta = 22.7^\circ$, as the slope angle α is varied in the range $0 \leq \alpha \leq 30^\circ$. This particular θ is also used for the majority of the experimental results reported in RKZS. $A_{\rm prim}$ is defined as the (dimensionless) maximum velocity of the reflected beam at 25 dimensionless units (about 20cm) from the reflection point A (see Fig. 1). For the parameter values Re = 103 and $\varepsilon = 0.2$ which correspond to the experiment of RKZS, the viscous solution for the primary reflected beam in Eqs.(32) is in satisfactory agreement with our numerical simulations. Under

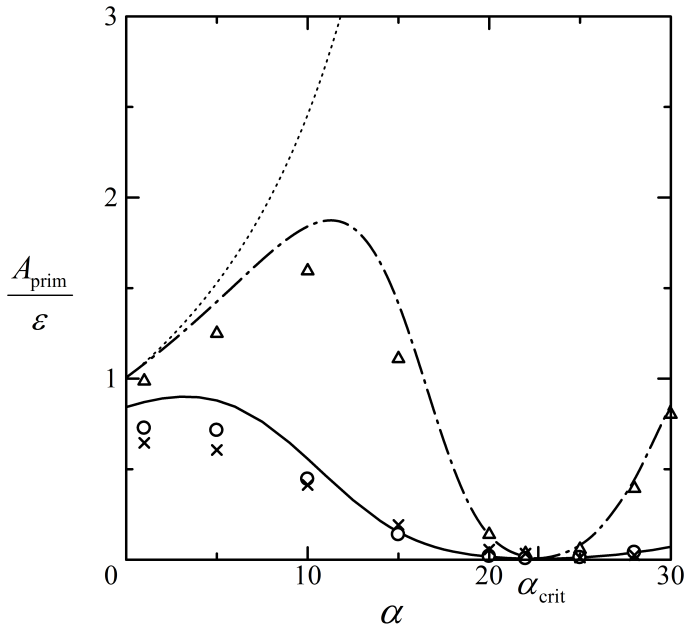

FIG. 2. Plots of normalized amplitude of primary-harmonic reflected beam as function of the slope angle $0 < \alpha < 30°$, for angle of incidence $\theta = 22.7°$ and two values of Re: solid line (Re = 103); dashed-dotted line (Re = 1030). The dotted line corresponds to the inviscid (Re = ∞) response, which features an infinite peak at $\alpha = \alpha_{\text{crit}} = \theta$. Symbols denote results of numerical simulations for certain values of Re and ε: $\times$ (Re = 103, $\varepsilon = 0.2$); $\bigcirc$ (Re = 103, $\varepsilon = 0.04$); $\triangle$ (Re = 1030, $\varepsilon = 0.04$).

these flow conditions, as suggested by the criterion in Eq.(13), viscous effects have a dominant role throughout the slope range $0 \leq \alpha \leq 30°$: the resonance peak at the critical slope angle $\alpha_{\text{crit}} = \theta = 22.7°$ predicted by the inviscid theory is completely suppressed, and the response exhibits a broad maximum within $0 \leq \alpha \lesssim 5°$. Overall, this viscosity-dominated response is also consistent with the results of numerical simulations in Fig. (10b) of RKZS. Furthermore, decreasing the incident wave amplitude ε to 0.04 for the same Re = 103 has a relatively minor effect, confirming that the linear viscous solution in Eqs.(32) is generally valid for small but finite ε. In contrast to ε, the response is quite sensitive to the choice of Re, as illustrated in Fig. 2 for the value Re = 1030, which is 10 times that in the experiment of RKZS. In this

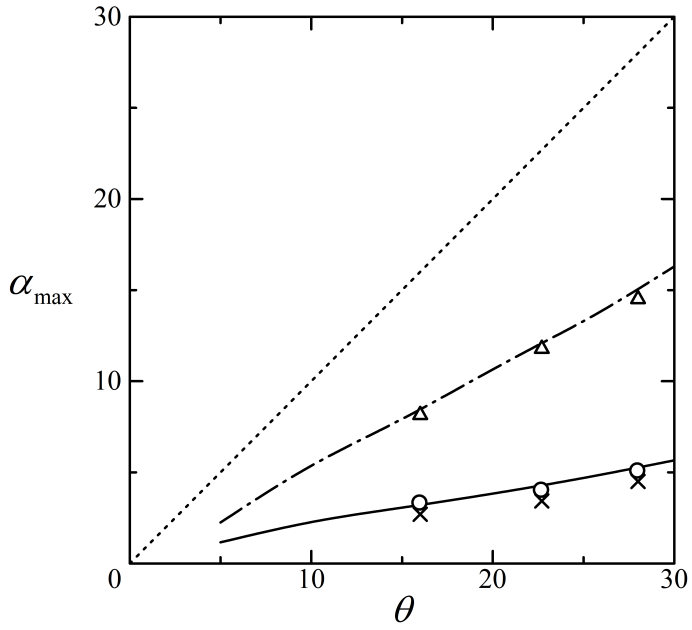

FIG. 3. Plots of the slope angle $\alpha_{\max}$ at which the primary-harmonic reflected beam attains the maximum amplitude as function of the incidence angle $5^\circ < \theta < 30^\circ$, for two values of Re: solid line (Re = 103); dashed-dotted line (Re = 1030). The dotted line indicates the inviscid limit (Re = ∞), where $\alpha_{\max} = \theta$. Symbols denote results of numerical simulations for certain values of Re and ε: $\times$ (Re = 103, $\varepsilon = 0.2$); $\bigcirc$ (Re = 103, $\varepsilon = 0.008$); $\triangle$ (Re = 1030, $\varepsilon = 0.008$).

instance, there is again reasonable agreement between theory and simulation. However, while viscous effects still dominate near $\alpha = \alpha_{\rm crit}$, here the response follows closely the inviscid result for $0 \leq \alpha \lesssim 7^\circ$ and features a relatively sharp peak around $\alpha = 12^\circ$. As Re is further increased so viscous effects become less important, the range of α where inviscid theory holds is expected to expand. In addition, the response peak would be steeper and occur closer to the critical angle $\alpha_{\rm crit} = \theta$, where viscosity cannot be ignored according to Eq.(13).

The primary-harmonic response discussed above for the incidence angle $\theta = 22.7^\circ$ is typical of reflections at other θ. Figure 3 shows plots for different Re and ε of the slope angle $\alpha = \alpha_{\max}$ at which $A_{\rm prim}/\varepsilon$ attains its maximum for given $5^\circ \leq \theta \leq 30^\circ$. The theoretical predictions

are generally in good agreement with the numerical simulations and confirm that as Re is increased $\alpha_{\max}$ approaches the critical angle $\alpha_{\rm crit} = \theta$ from below. Furthermore, varying the incident wave amplitude ε has little effect on $\alpha_{\max}$.

B. Second-harmonic response

Figure 4 shows theoretical plots and simulation results for the amplitude of the radiated second-harmonic beam $A_{\rm 2nd}$ (normalized with ε^2, as suggested by the weakly nonlinear expansion in Eq.(33)) when the slope angle α is varied in $0 \leq \alpha \leq 30^\circ$, for the same as in Fig. 2 incidence angle $\theta = 22.7^\circ$ as well as Re and ε. Similar to $A_{\rm prim}$, $A_{\rm 2nd}$ denotes the maximum velocity of the second-harmonic beam 25 dimensionless units (about 20cm) away from the reflection point A (see Fig. 1). Overall, the second-harmonic response exhibits qualitatively similar behavior to the primary reflected beam (see Fig. 2). For the experimental conditions of RKZS, where Re = 103 and $\varepsilon = 0.2$, again viscous effects dominate throughout $0 \leq \alpha \leq 30^\circ$, and the resonance peak of inviscid theory at $\alpha_{\rm crit} = \theta = 22.7^\circ$ is replaced by a bell-shaped curve with a broad maximum around $\alpha \approx 10^\circ$. By contrast, when Re is increased by a factor of 10, the second-harmonic amplitude is in close agreement with the inviscid limit for $0 \leq \alpha \lesssim 10^\circ$ and a relatively sharp peak forms at $\alpha \approx 21^\circ$, slightly below $\alpha_{\rm crit}$. Thus, in the limit ${\rm Re} \gg 1$, the response is expected to closely follow the inviscid result except in the immediate vicinity of $\alpha_{\rm crit}$ where viscous effects are always important.

The theoretical plots in Fig. 4 are generally in good qualitative, and in certain cases quantitative, agreement with the results of numerical simulations. The latter indicate that $A_{\rm 2nd} \propto \varepsilon^2$ holds for sufficiently small ε only. For Re = 103, in particular, we find good

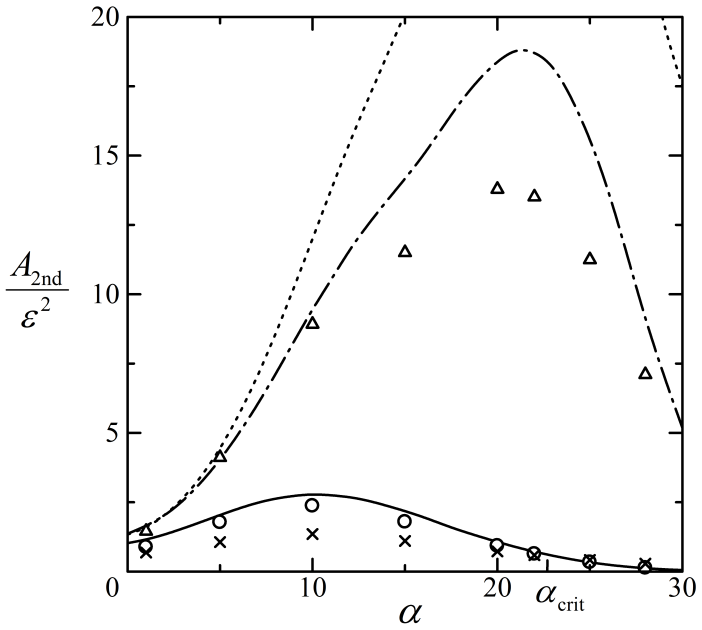

FIG. 4. Plots of normalized amplitude of second-harmonic radiated beam as function of the slope angle $0 < \alpha < 30°$, for angle of incidence $\theta = 22.7°$ and two values of Re: solid line (Re = 103); dashed-dotted line (Re = 1030). The dotted line corresponds to the inviscid (Re = ∞) response of Ref. [14], which features an infinite peak at $\alpha = \alpha_{crit} = \theta$. Symbols denote results of numerical simulations for certain values of Re and ε: × (Re = 103, $\varepsilon = 0.2$); ◯ (Re = 103, $\varepsilon = 0.04$); △ (Re = 1030, $\varepsilon = 0.04$).

agreement between theory and numerics for $\varepsilon = 0.04$, but for the 5 times larger value of $\varepsilon = 0.2$ as in the experiment of RKZS, the weakly nonlinear theory overestimates the second-harmonic amplitude roughly by a factor of 2.

For other incidence angles θ, the second-harmonic response exhibits the same behavior qualitatively as that in Fig. 4. Specifically, Fig. 5 illustrates, for different Re and ε, the dependence on θ of the slope angle $\alpha = \alpha_{max}^{2nd}$ at which A_{2nd}/ε^2 attains its maximum value when $0 < \alpha < 30°$. Similar to α_{max} for the primary reflected beam (see Fig. 3), α_{max}^{2nd} is controlled mainly by Re. Furthermore, α_{max}^{2nd} is found below $\alpha_{crit} = \theta$, where the inviscid second-harmonic response features a resonance peak. In addition, the incident wave amplitude

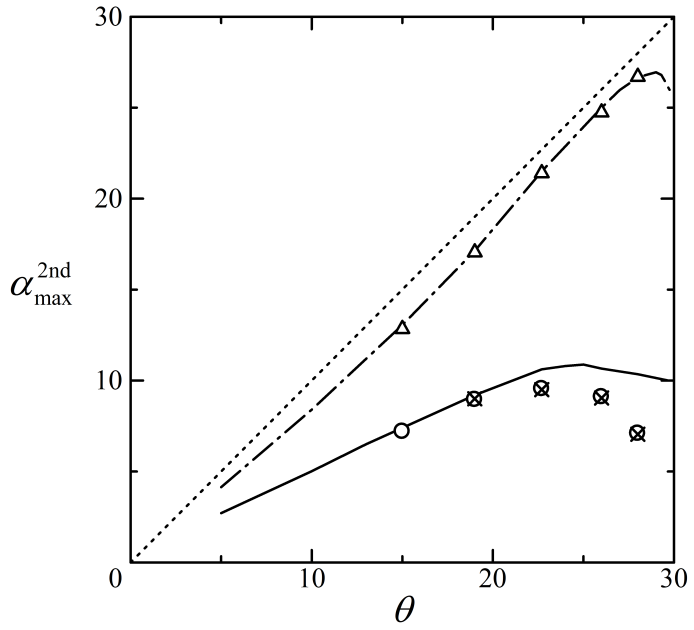

FIG. 5. Plots of the slope angle $\alpha_{\max}^{2\mathrm{nd}}$ at which the second-harmonic radiated beam attains the maximum amplitude as function of the incidence angle $5^\circ < \theta < 30^\circ$, for two values of Re: solid line (Re = 103); dashed-dotted line (Re = 1030). The dotted line indicates the inviscid limit (Re = ∞), where $\alpha_{\max}^{2\mathrm{nd}} = \theta$. Symbols denote results of numerical simulations for certain values of Re and ε: $\times$ (Re = 103, $\varepsilon = 0.2$); $\bigcirc$ (Re = 103, $\varepsilon = 0.008$); $\triangle$ (Re = 1030, $\varepsilon = 0.008$).

ε has relatively little effect on $\alpha_{\max}^{2\mathrm{nd}}$.

C. Comparison with the experiment of RKZS

The focus of the laboratory experiments of RKZS was on determining the slope angle that gives the most intense second-harmonic beam due to a primary beam incident at fixed angle θ to the horizontal. To this end, as a measure of the generated beam intensity, RKZS computed the integral of the square of the velocity amplitude over a suitably defined region along the second-harmonic beam. Based on this definition, their experimental data for $\theta = 22.7^\circ$ and $0 < \alpha < 25^\circ$ indicate that the beam intensity behaves as a bell-shaped function with peak at

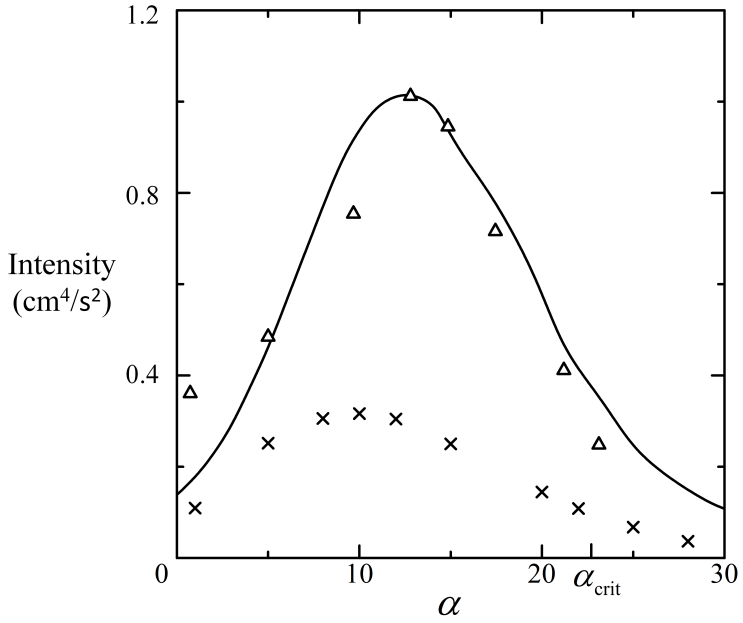

FIG. 6. Intensity of radiated second-harmonic beam as function of slope angle $0 < \alpha < 30°$ for incidence angle $\theta = 22.7°$, under the flow conditions of RKZS (Re = 103 and $\varepsilon = 0.2$). The solid line corresponds to the theoretical predictions. The crosses are results of numerical simulations. The open triangles denote the experimental results in Fig. 7 of RKZS after being multiplied by the constant factor 0.1 such that the peak value at $\alpha = 13.2°$ matches the theoretical intensity estimate at this α.

$\alpha = 13.2°$. We attempted detailed comparison of these experimental results with our weakly nonlinear viscous theory by computing theoretical estimates for the second-harmonic beam intensity according to the definition in RKZS. The theoretical results show similar qualitative behavior to the observations as α is varied and predict a maximum close to the experimental value $\alpha = 13.2°$ (see Fig. 6). Quantitatively, however, the theoretical intensity predictions turn out to be typically 10 times smaller than the experimental values reported in Fig. 7 of RKZS. On the other hand, as shown in Fig. 6, we find very good quantitative agreement between experiment and theory if the experimental intensity results in Fig. 7 of RKZS are multiplied by the constant factor 0.1 such that the peak value at $\alpha = 13.2°$ matches the

theoretical intensity estimate at this α. Figure 6 also shows computed values of the second-harmonic beam intensity based on the velocity fields obtained from our numerical simulations. The numerical estimates for the second-harmonic intensity feature a broad maximum around $\alpha \simeq 10^\circ$ and are smaller, roughly by a factor of 3–4, than the predictions of the theoretical model. This seems reasonable considering that the weakly nonlinear theory for $\varepsilon = 0.2$ overestimates the numerical second-harmonic amplitudes roughly by a factor of 2 (see Fig. 4) and that the intensity involves the square of the beam amplitude.

In an effort to shed light on the cause of the quantitative discrepancy between the experimental and our theoretical/numerical estimates for the second-harmonic intensity, it was first verified that the incident beam profile matched to a good approximation the experimental one in Fig. 4 of RKZS. Secondly, we made a comparison of our theoretical and numerical results for the square of the second-harmonic amplitude with the contour plot of the measured data (for $\theta = 22.7^\circ$, $\alpha = 20^\circ$) in Fig. 5 of RKZS. We found overall good agreement between the numerical results and the experimental observations, while as expected the predictions of the theoretical model were generally higher roughly by a factor of 4. These findings suggest that the discrepancy between the experimental intensity values reported in Fig. 7 of RKZS and the theoretical (by a factor of 10) as well as the numerical (roughly by a factor of 3) results, is likely due to a different interpretation of the ad hoc method used by RKZS for determining the intensity. This possible explanation is also hinted by the units of beam intensity stated in Fig. 7 of RKZS, $\mathrm{cm}^2/\mathrm{s}^2$, which are inconsistent with the expected units, $\mathrm{cm}^4/\mathrm{s}^2$, based on the definition of beam intensity as the integral of the square of the velocity amplitude over a certain area.

VI. CONCLUDING REMARKS

We have extended the inviscid weakly nonlinear model of Tabaei et al. [14] to account for viscous dissipation in the reflection of a locally confined internal wave beam from a uniform slope. Asymptotically, at high Reynolds number, viscous effects are expected to come into play predominantly in the immediate vicinity of the critical condition where the beam angle of incidence matches the slope angle. However, for quantitative comparison against laboratory experiments where the Reynolds number is moderately large, it may be necessary to include viscosity for a broad range of flow conditions. According to our model, the main effect of viscosity for both the primary- and second-harmonic reflected beams is to replace the sharp (theoretically infinite) resonance peaks of the inviscid responses at the critical condition with bell-shaped finite peaks at slope angles below the critical. Under the experimental flow conditions of RKZS, this viscous modification turns out to be quite significant as it affects the reflected beam amplitudes throughout the range of slope angles considered in these experiments, which explains why the agreement with the inviscid theory of Tabaei et al. [14] is poor. The predictions of the proposed model, by contrast, are generally consistent with the experimental observations, with the exception of the values of the second-harmonic intensity as defined in RKZS, which appear to be off by a constant scaling factor for reasons that are presently unknown. Finally, here it has been assumed that the incident beam planes of constant phase meet the slope along the isobaths so the flow is two-dimensional. In the case of oblique reflection [24], the induced mean flow has a more prominent presence, and including viscous effects would require a separate, more elaborate theory.

ACKNOWLEDGEMENTS

This work was supported by the NSF under Grant No. DMS-1512925 and in part by Kobe University Complex Fluid and Thermal Engineering Research Center.

---

[1] O. M. Phillips, *The Dynamics of the Upper Ocean* (Cambridge University Press, 1966).

[2] D. Cacchione and C. Wunsch, Experimental study of internal waves over a slope, J. Fluid Mech. **66**, 223 (1974).

[3] G. N. Ivey and R. I. Nokes, Vertical mixing due to the breaking of critical internal waves on sloping boundaries, J. Fluid Mech. **204**, 479 (1989).

[4] C. C. Eriksen, Implications of ocean bottom reflection for internal wave spectra and mixing, J. Phys. Oceanogr. **15**, 1145 (1985).

[5] C. Wunsch and R. Ferrari, Vertical mixing, energy, and the general circulation of the oceans, Annu. Rev. Fluid Mech. **36**, 281 (2004).

[6] T. Dauxois and W. R. Young, Near-critical reflection of internal waves, J. Fluid Mech. **390**, 271 (1999).

[7] T. Dauxois, A. Didier, and E. Falcon, Observation of near-critical reflection of internal waves in a stably stratified fluid, Phys. Fluids **16**, 1936 (2004).

[8] V. K. Chalamalla, B. Gayen, A. Scotti, and S. Sarkar, Turbulence during the reflection of internal gravity waves at critical and near-critical slopes, J. Fluid Mech. **729**, 47 (2013).

[9] A. Tabaei and T. R. Akylas, Nonlinear internal gravity wave beams, J. Fluid Mech. **482**, 141 (2003).

[10] A. Tabaei, Theoretical and experimental study of nonlinear internal gravity wave beams, Ph.D. thesis, Massachusetts Institute of Technology (2005).

[11] S. A. Thorpe, On the reflection of a train of finite-amplitude internal waves from a uniform slope, J. Fluid Mech. **178**, 279 (1987).

[12] M. Leclair, K. Raja, and C. Staquet, Nonlinear reflection of a two-dimensional finite-width internal gravity wave onto a slope, J. Fluid Mech., to appear.

[13] K. G. Lamb, Nonlinear interaction among internal wave beams generated by tidal flow over supercritical topography, Geophys. Res. Lett. **31**, L09313 (2004).

[14] A. Tabaei, T. R. Akylas, and K. G. Lamb, Nonlinear effects in reflecting and colliding internal wave beams, J. Fluid Mech. **526**, 217 (2005).

[15] T. Peacock and A. Tabaei, Visualization of nonlinear effects in reflecting internal wave beams, Phys. Fluids **17**, 061702 (2005).

[16] L. Gostiaux, T. Dauxois, H. Didelle, J. Sommeria, and S. Viboud, Quantitative laboratory observations of internal wave reflection on ascending slopes, Phys. Fluids **18**, 056602 (2006).

[17] I. Pairaud, C. Staquet, J. Sommeria, and M. M. Mahdizadeh, Generation of harmonics and sub-harmonics from an internal tide in a uniformly stratified fluid: numerical and laboratory experiments, in *IUTAM Symposium on Turbulence in the Atmosphere and Oceans*, Vol. 28, edited by D. Dritschel (IUTAM Bookseries, 2010) pp. 51–62.

[18] T. Gerkema, C. Staquet, and P. Bouruet-Aubertot, Decay of semi-diurnal internal-tide beams due to subharmonic resonance, Geophys. Res. Lett. **33**, L08604 (2006).

[19] B. Rodenborn, D. Kiefer, H. P. Zhang, and H. L. Swinney, Harmonic generation by reflecting internal waves, Phys. Fluids **23**, 026601 (2011).

[20] L. Gostiaux, H. Didelle, S. Mercier, and T. Dauxois, A novel internal waves generator, Exps. Fluids **42**, 123 (2007).

[21] M. J. Mercier, D. Martinand, M. Mathur, L. Gostiaux, T. Peacock, and T. Dauxois, New wave generation, J. Fluid Mech. **657**, 308 (2010).

[22] A. A. Aksu, Nonlinear viscous higher harmonics generation due to incident and reflecting internal

wave beam collision, Phys. Fluids **29**, 096603 (2017).

[23] F. H. Harlow and J. E. Welch, Numerical calculation of time-dependent viscous incompressible flow of fluid with free surface, Phys. Fluids **8**, 2182 (1965).

[24] T. Kataoka and T. R. Akylas, On mean flow generation due to oblique reflection of internal waves at a slope, Stud. Appl. Math. **142**, 419 (2019).